




Electrophysiological characterization of pre-adolescents born with intrauterine growth restriction: insights from clinical and computational data

Freddy L. Bueno-Palomeque^{1,2,3} , Ernesto Zacur⁴, Esther Pueyo^{1,2}, Fàtima Crispí⁵ , Pablo Laguna^{1,2}  and Ana Mincholé^{1,2}

¹BSICoS Group, I3A, IIS Aragón, Universidad de Zaragoza, C/Mariano Esquillor s/n, Zaragoza, Spain

²CIBER en Bioingeniería, Biomateriales y Nanomedicina (CIBER-BBN), C/Monforte de Lemos 3-5, Madrid, Spain

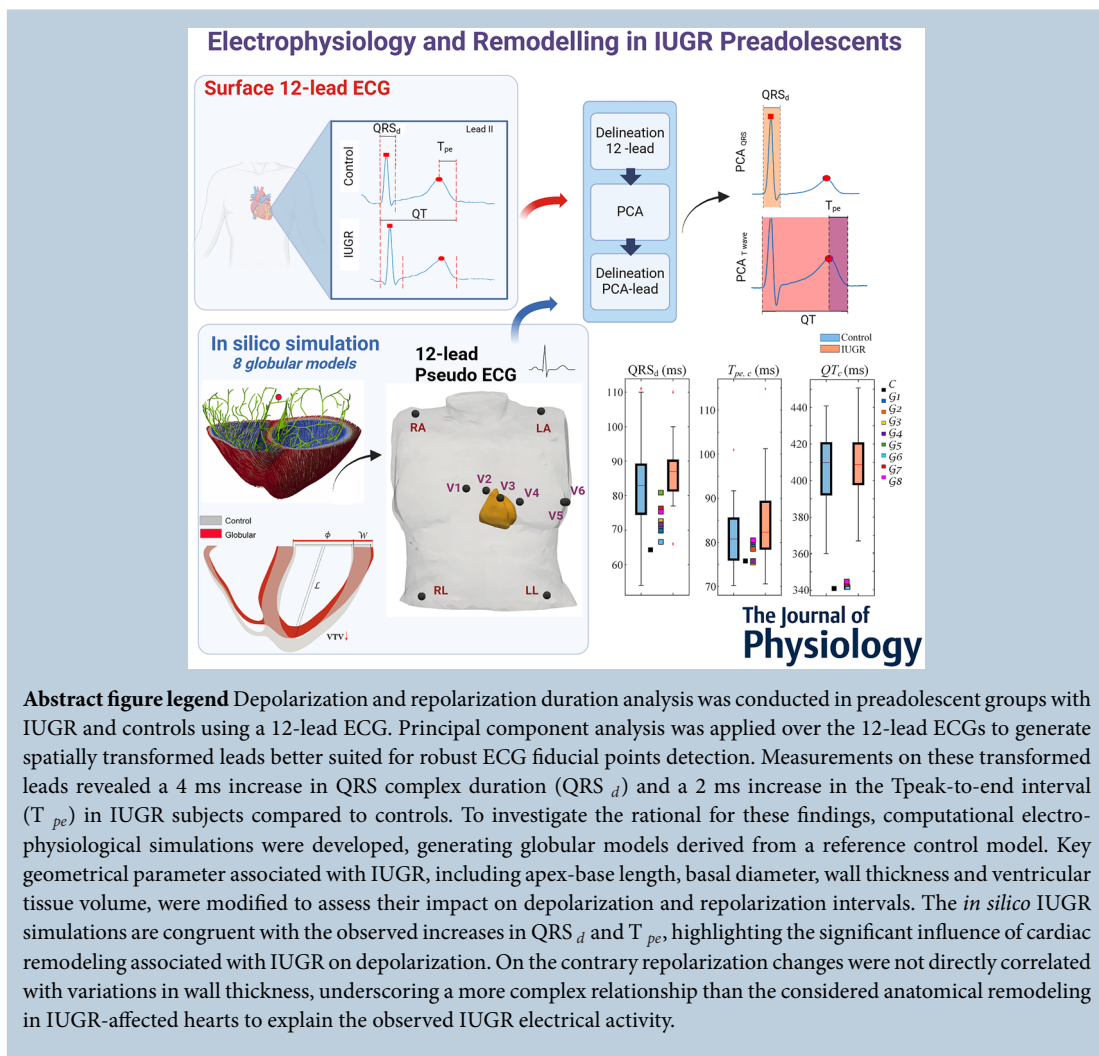
³GIHEA, Universidad Politécnica Salesiana, C/Vieja 12-30, Cuenca, Azuay, Ecuador

⁴Corify Care SL, C/Dr. Castelo, 44, Madrid, Spain

⁵BCNatal – Barcelona Center for Maternal-Fetal and Neonatal Medicine, Hospital Sant Joan de Déu and Hospital Clínic, University of Barcelona, Barcelona, Spain

Handling Editors: Bjorn Knollmann & Axel Loewe

The peer review history is available in the Supporting Information section of this article (<https://doi.org/10.1113/JP288197#support-information-section>).



Abstract Anatomical changes associated with intra-uterine growth restriction (IUGR) have been observed in different age groups and linked to cardiovascular complications. This study analysed the electrocardiogram (ECG) in pre-adolescents with severe IUGR, comparing QRS complex and T-wave biomarkers with controls. Computer simulations explored links between anatomical re-modelling and ECG biomarkers, providing insights into the potential cardiovascular risk associated with IUGR-induced re-modelling. Clinical recordings were analysed using principal component analysis (PCA) to compute spatially transformed leads, enhancing QRS complex and T-wave delineation for depolarization and repolarization assessment. Transformed leads analysis revealed a 4-ms increase in QRS complex duration (QRS_d) and a 2-ms increase in the T peak-to-end interval (T_{pe}) in IUGR subjects compared to controls. We conducted electrophysiological *in silico* simulations using anatomical models based on clinical IUGR data. These models, derived from a reference control, incorporated key geometric changes associated with IUGR, the apex-base length, basal diameter, wall thickness (W) and ventricular tissue volume, to assess their impact on depolarization and repolarization intervals. *In silico* PCA leads showed increased QRS_d , QRS amplitude and T_{pe} in globular models, consistent with clinical data. Despite the QRS_d increase, the QT interval increases but is not linearly related to the W change. These findings suggest that cardiac re-modelling primarily influences the depolarization cycle, notably QRS_d , while repolarization intervals increase but are not directly related to the W increase. The study highlights the impact of geometric and volumetric changes in IUGR-related cardiac re-modelling, also emphasizing the need for further research on electrophysiological re-modelling and its effects on cardiac function.

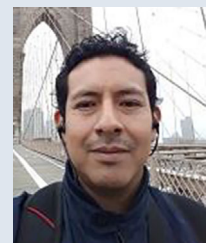
(Received 27 November 2024; accepted after revision 12 May 2025; first published online 5 June 2025)

Corresponding author Freddy L. Bueno-Palomeque, BSICoS Group, I3A, IIS Aragón, Universidad de Zaragoza, C/ Mariano Esquillor s/n, Zaragoza, 50018, Spain. Email: 812750@unizar.es

Key points

- Intrauterine growth restriction (IUGR) is associated with long-term cardiovascular complications, including changes in the heart's electrical activity.
- Cardiac re-modelling as a consequence of IUGR can lead to electrical changes that can be assessed through an electrocardiogram (ECG).
- This study analysed ECGs in pre-adolescents with severe IUGR, revealing prolonged depolarization duration (QRS complex duration) and repolarization (T peak-to-end interval) compared to healthy controls.
- Computational models incorporating clinically observed anatomical changes, such as increased ventricular wall thickness and altered heart geometry, were used to assess their impact on electrical function, and determine whether these structural modifications contribute to the ECG alterations observed in clinical data.
- Both clinical data analysis and simulation findings showed significant shifts in depolarization-based biomarkers and smaller, and non-linear changes to geometrical changes, in repolarization intervals, highlighting how cardiac re-modelling in IUGR affects heart function as measured by ECG.

Leonardo Bueno was born in Cuenca, Ecuador, in 1983. He received the Master's degree in Biomedical Engineering from the Universidad Nacional de Colombia in 2013, collaborating with the Biomechanical Research group in the Virtual Surgery Scenarios Project. He is currently a full time professor in the Universidad Politécnica Salesiana in Ecuador and he is working on the Ph.D. degree in Biomedical Engineering in the University of Zaragoza. His research interests include the field of biomedical signal processing and computational models.



Introduction

Cardiovascular diseases are among the leading causes of death in adults worldwide, with some conditions originating from congenital factors. Low birth weight has been identified as one contributing factor linked to heart problems in adulthood, with intra-uterine growth restriction (IUGR) recognized as a primary cause (Barker, 1990). IUGR is an obstetric condition that affects 7%–10% of fetuses during pregnancy, with a higher occurrence (De Onis et al., 1998) in underdeveloped/developing countries compared to developed nations. IUGR has been associated with other adult diseases in both human epidemiological studies and animal models. In some cases, intrauterine deprivation programmes the fetus to develop increased appetite and obesity, hypertension and diabetes as an adult. Although the mechanisms responsible for fetal programming remain poorly understood, both anatomical and functional (cell signalling) changes have been described in affected individuals (Ross & Beall, 2008). The consequences of IUGR include an increased risk of cardiovascular disease later in life (Sharma et al., 2016; Visentin et al., 2014).

Among the consequences of IUGR, cardiac remodelling has been observed (Cruz-Lemini et al., 2016; Crispi et al., 2020; Sarvari et al., 2017), affecting the ventricular sphericity index (SpI), which is the ratio of apex-base length (L) to basal diameter (ϕ), $SpI = L/\phi$, primarily in the left ventricle (Zaharie et al., 2019). This morphological remodelling has been observed in both newborns and pre-adolescents (8–12 years) (Sarvari et al., 2017), although its persistence into adulthood appears to be subtle (Arnott et al., 2015). In addition, studies in adults suggest that individuals who experienced restricted growth during fetal and early childhood stages exhibit greater left ventricular mass, particularly affecting the interventricular septum and left posterior wall. This is reflected in a significant increase in the relative wall thickness in the IUGR cohort (Vijayakumar et al., 1995), which has also been observed in pre-adolescents diagnosed with severe IUGR (Sarvari et al., 2017). Another study in adults born at term with a history of IUGR reported a significant reduction in basal left ventricular diameter in the IUGR cohort, but no differences in posterior ventricular wall thickness (Bjarnegård et al., 2013).

Regarding electrophysiology, clinical data from pre-adolescents have shown differences in the dominant vectors of depolarization and repolarization across the three spatial planes of a vectorcardiogram (Ortigosa et al., 2016), findings that are supported by *in silico* simulations (Bueno-Palomeque et al., 2020). Similar electrical alterations have also been observed in adults (Ortigosa et al., 2018). Moreover, *in silico* studies highlight significant shifts in the direction of dominant

vectors due to geometric re-modelling, though some discrepancies remain when compared to clinical results (Bueno-Palomeque et al., 2023a).

The QRS complex duration (QRS_d) obtained from the standard 12-lead electrocardiogram (ECG) is a key marker associated with morphophysiological abnormalities and has been shown to predict congestive heart failure (Ilkhanoff et al., 2012), incidents of atrial fibrillation (Aeschbacher et al., 2018) and death. During the fetal stage QRS_d measurements in an IUGR cohort (26 pregnant women) were found to be two standard deviations below the normal value seen in AGA (appropriate for gestational age) fetuses, as measured through ECG recorded from the maternal surface within 10 days before delivery (Brambati & Bonsignore, 1982). Similar findings were found in Pardi's study, where 54 out of 68 fetuses were classified as IUGR, and 44 of them showed a QRS_d two standard deviations smaller than the normal mean value for their gestational age (Pardi & Marconi, 1986). In contrast, Grimm's study, which assessed QRS complex intervals using fetal magnetocardiography in a cohort of 30 IUGR subjects and 60 controls, found a non-significant increase in QRS_d (Grimm et al., 2003). Similarly, Van Leeuwen's study reported significantly longer QRS_d in an IUGR cohort measured using fetal magnetocardiography (Van Leeuwen et al., 2001). In addition, Velayo's study found no significant difference in QRS_d between the IUGR (15 subjects) and control cohorts (20 subjects) using trans-abdominal fetal ECG (Velayo et al., 2017).

During the repolarization phase, the QT and the T-peak-to-end (T_{pe}) intervals are important indicators of ventricular arrhythmias in severe cardiac conditions (Yamaguchi et al., 2003). In the fetal stage, a study found that the QT interval was significantly prolonged in the IUGR cohort compared to controls, as determined by transabdominal fetal ECG (Velayo et al., 2017). Variability in the repolarization segment has also been observed in a cohort of neonates, with greater dispersion in both QT and JT intervals observed within the IUGR cohort (Fouzas et al., 2014), strengthening the relationship between IUGR and ECG alterations. In addition, the T_{pe}/QT ratio serves as an index of arrhythmogenesis, reflecting the relationship between repolarization dispersion and ventricular action potential durations (APD) (Gupta et al., 2008). Changes in the T-wave morphology are linked to action potential (AP) changes across the ventricles (Emori & Antzelevitch, 2001).

In this study we analysed ECG signals from a cohort of preadolescents diagnosed with severe IUGR, providing an opportunity to investigate whether the changes in biomarkers reported during the newborn stage persist into later developmental stages. Although depolarization and repolarization biomarkers exhibited variations related to IUGR, the relationship between IUGR-induced geometric re-modelling and changes in these electrophysiological

biomarkers remains unclear. Furthermore the underlying mechanisms driving these variations are also not well understood.

We hypothesize that the anatomical alterations in the basal diameter ϕ and the widening of the ventricular wall thickness (\mathcal{W}) may impact the morphology of both the QRS complex and the T-wave.

The primary aim of this study was to compare and characterize control and IUGR preadolescent subjects using different ECG-based depolarization and repolarization biomarkers related to arrhythmia susceptibility. In addition we aimed to assess *in silico* how IUGR-induced anatomical re-modelling, including a reduction in the SpI and variations in wall thickness \mathcal{W} , affects these ECG biomarkers.

Materials and methods

Ethical approval and clinical data

The study involved the measurement of ECG intervals during both depolarization and repolarization phases using 12-lead surface ECG recordings. The study population included 93 pre-adolescents (from 8 to 12 years old), divided into two cohorts. The control cohort consisted of 60 term-born subjects with normal growth profiles, whereas the IUGR cohort comprised 33 subjects diagnosed with severe IUGR and who underwent medically induced delivery. IUGR was defined as a birth weight below the 10th percentile for gestational age combined with an abnormal umbilical artery Doppler, indicated by a pulsatility index above the 95th percentile. Adequate growth was considered when a birth weight above the 10th percentile for gestational age occurs, based on standards in Figueras et al. (2008).

The study population was described in a previously published cohort study, conducted at a tertiary university hospital in Barcelona, Spain (Crispi et al., 2010). The study conformed to the standards set by the Declaration of Helsinki, except for registration in a database. The study was approved by the Hospital Clinic Ethics Committee (Ref: HCB2014/0598), and written parental consent was obtained. For each subject, a 13-s ECG recording sampled at 1000 Hz was collected. ECG data used in this study are available under reasonable request from the authors of the clinical data acquisition study described in Crispi et al. (2010).

ECG signal processing and the computation of biomarkers

The ECG signals were filtered and delineated using a wavelet-based delineator (Martínez et al., 2004). The onset and end of the QRS complex and T-wave were

identified using a single-lead delineation approach with a multilead-based rule technique that provided accurate lead-independent delineation marks for each beat. This first stage was used to identify and segment the QRS complex and the T-wave. However, the detection of characteristic ECG points, and consequently the derived interval values, can vary across leads due to poor delineation in leads with a low signal-to-noise ratio (SNR), or differences in the projections of electrical activity at different leads. To reduce this variability, and achieve robust and lead-independent measurements, we used two synthesized leads derived as optimal linear combinations of standard leads using principal component analysis (PCA) (Castells et al., 2007). This approach maximizes the SNR, thereby improving the precision of wave boundary identification. Furthermore, using a lead-independent measure is particularly advantageous when comparing records where electrode (lead) placement consistency cannot be guaranteed. This ensures more robust and reliable comparisons across different recordings.

Two transformed leads, one emphasizing the QRS complex, PCA_{QRS} , and the other emphasizing the T-wave, PCA_{T} , were generated. The PCA coefficients for lead PCA_{QRS} were learned within the QRS complex area when QRS delineation is the target, whereas the PCA_{T} coefficients are learned within the T-wave region when delineating the T-wave. PCA separates the orthogonal components of the $L = 8$ independent leads in descending order of variance (Castells et al., 2007). The matrix Ψ_{PCA} defining the transformation was obtained (learned) from the eigenvectors of the 8×8 inter-lead ECG auto-correlation matrix computed using the samples in the QRS complex (or T-waves) (Castells et al., 2007; Ramírez et al., 2017) within the corresponding learning window, for PCA_{QRS} (or PCA_{T}). As a result, the transformed lead derived coming from the first PCA component is the lead maximizing the energy of the QRS complex (PCA_{QRS}) or T-wave (PCA_{T}) energy. To illustrate the computation of the transformation matrix Ψ_{PCA} , let K be the number of segmented and aligned T-waves (or QRS complexes) within the learning window, each consisting of N samples, across L available leads. Let $x_{k,l}(n)$ denote the n th selected sample of the k th beat in the l th lead of the filtered ECG signal. In vector notation, the T-wave (or QRS complex) from the k th beat of the l th lead is represented as: $\mathbf{x}_{k,l} = [x_{k,l}(0) \cdots x_{k,l}(N-1)]^T$; these vectors are then stacked together into an $L \times N$ matrix \mathbf{X}_k , and further into \mathbb{X} as,

$$\mathbf{X}_k = [\mathbf{x}_{k,1} \mathbf{x}_{k,2} \cdots \mathbf{x}_{k,L}]^T \quad \text{and} \quad \mathbb{X} = [\mathbf{X}_1 \mathbf{X}_2 \cdots \mathbf{X}_K], \quad (1)$$

where the n th column of \mathbf{X}_k contains the amplitudes of the L leads at a given sample n . Data matrix \mathbb{X} is then constructed by concatenating K consecutive matrices \mathbf{X}_k .

To maximize the signal energy at the transform leads, it is known that the 8×8 transform matrix $\Psi_{\text{PCA}} = [\psi_1 \ \psi_2 \ \cdots \ \psi_8]$ should accomplish the following equation:

$$\mathbf{R}_{\mathbf{X}} \Psi_{\text{PCA}} = \Psi_{\text{PCA}} \mathbf{\Lambda}, \quad \text{with} \quad \mathbf{R}_{\mathbf{X}} = \frac{1}{\text{KN}} \mathbf{X} \mathbf{X}^T \quad (2)$$

being the spatial correlation matrix of \mathbf{X} , and $\mathbf{\Lambda}$ a diagonal matrix containing the eigenvalues of $\mathbf{R}_{\mathbf{X}}$ at the diagonal.

If $\mathbf{x}(n) = [x_1(n) \ x_2(n) \ \cdots \ x_L(n)]^T$, where $x_l(n)$ represents the ECG signal samples at l th lead, then in matrix notation, $\mathbf{x}(n)$ represents the multilead ECG signal at the n th sample. The first transformed lead (PCA_{QRS} or PCA_T) is then given by

$$\text{PCA}(n) = \psi_1^T \mathbf{x}(n). \quad (3)$$

These transformed leads were delineated to identify the beginning, peak and end points, with lead PCA_{QRS} used for the QRS complex and lead PCA_T for the T-wave, as these leads are better suited for each case, as illustrated in Fig. 1.

Subsequently, the median value of the QRS_d across beats was calculated and considered representative for each patient. The T_{pe} and QT intervals were measured in each beat in lead PCA_T and corrected using Fridericia's formula ($T_{pe,c} = T_{pe}/\sqrt[3]{RR}$ and $QT_c = QT/\sqrt[3]{RR}$), being RR the interval between QRS complex peaks of current and preceding beat. With these corrected parameters, the T_{pe,c}/QT_c ratio was also determined. The medians across beats of T_{pe,c}, QT_c and T_{pe,c}/QT_c were then taken as representatives for each patient. Manual delineation was conducted in the PCA_{QRS} lead of two subjects, focusing on the QRS complex onset, as the markers were erroneously placed at the peak of the Q-wave rather than at its onset. The results for the control and IUGR cohorts were statistically compared using the Student's *t*-test once it was verified that they had a normal distribution.

Computational modelling of human electrophysiology

A realistic biventricular heart within a torso model was used for this study (Martinez-Navarro et al., 2019) as the control model (C), and was later deformed to generate globular IUGR models (G). The C model was meshed using tetrahedral elements ($\sim 330,000$ nodes and $\sim 2,000,000$ elements). The O'Hara-Rudy (ORd) AP model for healthy tissue (Dutta et al., 2017; O'Hara et al., 2011) was used to simulate the cellular electrophysiological behaviour of the ventricles. To model the propagation of electrical impulse across the myocardium, we utilized the monodomain model (Potse et al., 2006)

through the finite element method (Mountris et al., 2019), defined by the following reaction–diffusion equation:

$$\nabla \cdot (\mathbf{D} \nabla V_m) = \beta \left(C_m \frac{\partial V_m}{\partial t} + I_{\text{ion}} \right), \quad (4)$$

$$\mathbf{n} \cdot (\mathbf{D} \nabla V) = 0, \quad (5)$$

where \mathbf{D} is the diffusion tensor, V_m is the transmembrane potential, β is the surface-to-volume ratio of the cell membrane, C_m is the membrane capacitance and the boundary condition is 0 and I_{ion} is the current density flowing through the ionic channels.

Extracellular potentials were computed at the positions of virtual electrodes \mathbf{e} on a torso model to generate a virtual 12-lead ECG (Gima & Rudy, 2002). For this computation the heart is considered to be embedded within an infinite homogeneous volume conductor. The same torso electrode coordinates were used across all

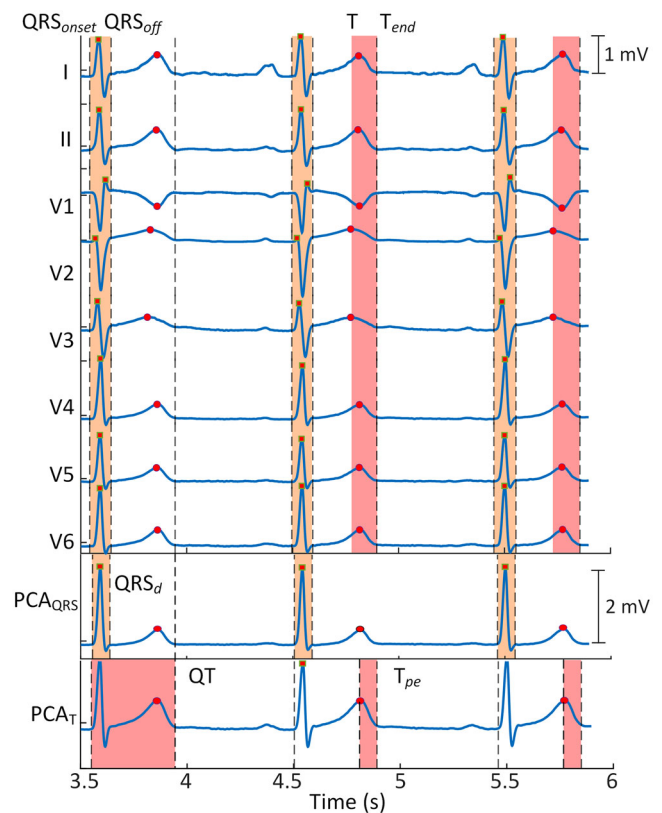


Figure 1. Identification and delineation of the QRS complex and T-wave across each of the eight electrocardiogram (ECG) leads of an ECG signal from a control group subject QRS complex and T peaks are marked with red squares and circles, respectively. The black dashed lines are aligned with the delineation marks of lead V2. Note that markers as T-wave peak differ across leads, making intervals lead dependent. At the bottom leads, QRS_d interval measured over PCA_{QRS} is shaded in orange and T_{pe} and QT intervals measured over PCA_T are shaded in red.

simulations. Extracellular potentials were then computed using the following equation:

$$\phi(\mathbf{e}, t) = \int_{\Omega} \left(-\mathbf{D} \cdot \nabla V_m \cdot \left(\nabla_{\mathbf{r}} \frac{1}{\|\mathbf{r} - \mathbf{e}\|} \right) \right) d\mathbf{r}, \quad (6)$$

where $\phi(\mathbf{e}, t)$ is the extracellular potential calculated at electrodes located at a point with spatial coordinates $\mathbf{e} = [e_x \ e_y \ e_z]$; \mathbf{D} is considered constant and homogeneous in this study; and $1/\|\mathbf{r} - \mathbf{e}\|$ represents the decay of the electric field with distance from source \mathbf{r} to electrode \mathbf{e} , and Ω is the volume where the tissue is located.

After pre-pacing the cellular model to achieve steady-state conditions, a sequence of three beats was simulated at a frequency of 60 bpm (RR = 1000 ms), using a stimulus amplitude of 200 mA with a 0.5-ms duration. The third beat was selected to ensure that the state variables involved in the cellular model reached steady-state conditions. A dual adaptive explicit time integration method as described in Mountris & Pueyo (2021) was used, with an adaptive time step ranging from 0.01 to 0.1 ms.

Electrophysiological propagation. The electrical propagation was initiated at the Bundle of His and fastly spread through the Purkinje network, which couples to the myocardium at discrete sites known as Purkinje-myocyte junctions (PMJs) (see Fig. 2A). The Purkinje network was generated using a fractal projection method (Costabal et al., 2016), incorporating a posterior main branch to achieve QRS complex morphologies within clinical ranges. To ensure the rapid electrical conduction at 2.9 m/s, a diffusion coefficient of $0.013 \text{ cm}^2/\text{ms}$ was set along the Purkinje network (Kléber et al., 2011). At the PMJs, this value was reduced to $0.0023 \text{ cm}^2/\text{ms}$, modelling the transition to the myocardial tissue. The Purkinje cellular AP was represented using the Stewart model (Stewart et al., 2009). The Purkinje network was meshed with an average edge length of $750 \text{ }\mu\text{m}$.

Within the myocardial tissue, electrical propagation followed a fibre architecture defined by a rule-based method (Doste et al., 2019). The fibre orientation exhibited a counterclockwise rotation from the apex to the base, with fibre angles gradually transitioning from -60° at the endocardium to $+60^\circ$ at the epicardium across both ventricles (see Fig. 2B). The myocardial tissue was modelled with orthotropic conductivity and transverse isotropy, that is, with identical conductivities in the sheet and normal-sheet directions. A transverse-to-longitudinal conductivity ratio of 0.25 was applied, introducing conduction velocity anisotropy consistent with experimentally observed cardiac tissue behaviour (Spach et al., 1981). The longitudinal diffusion coefficient was set at $0.0013 \text{ cm}^2/\text{ms}$, complemented by a membrane capacitance of $1 \text{ pF}/\text{cm}^2$. This configuration resulted in an average longitudinal conduction velocity of 0.67 m/s within the myocardium (Kléber et al., 2011).

First a fibre network was generated for the C model and later adapted to fit the modified endocardial surface of each of the G models, while maintaining the same number of nodes and segments across all models (~ 7000 nodes and elements). The onset of the electrical activation was set in all simulations at the same spatial point corresponding to the His bundle.

Transmural and apicobasal heterogeneities. Transmural ventricular heterogeneities were implemented in the ORD endocardial AP model by applying scaling factors to key ionic currents and properties, as described in O'Hara et al. (2011). The main differences in ionic currents include a pronounced transient outward potassium current (I_{to}) along with a higher rapid (I_{Kr}) and slow (I_{Ks}) rectifier potassium currents, resulting in the shortest APD observed experimentally in epicardial cells. Mid-myocardial cells exhibit the highest late sodium current (I_{NaL}), along with reduced I_{Kr} and I_{Ks} , leading to the longest APD of the three. Endocardial cells exhibit intermediate levels of these currents and APD (O'Hara et al., 2011).

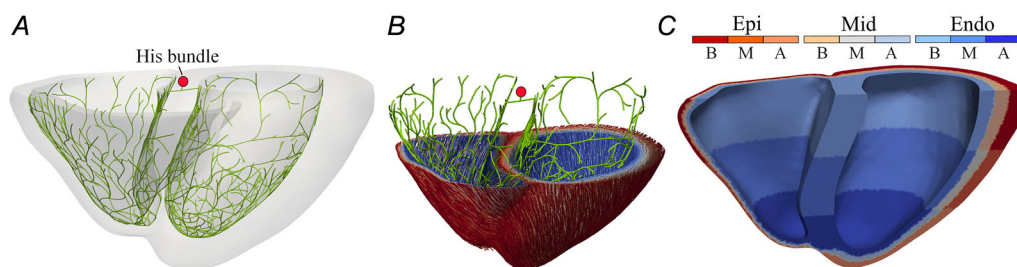


Figure 2. Electrophysiological features implemented. (A) Implementation of the Purkinje network on the endocardial surface of the models

The red circle indicates the His Bundle where electrical propagation begins. (B) Implementation of fibres and propagation direction at each node from the endocardial to the epicardial surface. (C) Division of the tissue into nine zones incorporating transmural (endo, mid and epi tissue) and apicobasal heterogeneities (base (B), middle (M) and apex (A)).

The spatial distribution of transmural heterogeneity in membrane kinetics was modelled by incorporating distinct endocardial, midmyocardial and epicardial cell layers with varying relative thicknesses (see Fig. 2C). Specifically the wall thickness was distributed such that 30% was allocated to endocardial cells, 30% to mid-myocardial cells and 40% to epicardial cells (Mincholé et al., 2019), with the interventricular septum modelled entirely as endocardial cells.

In addition, electrophysiological heterogeneities were introduced along the apex-to-base axis to reflect the longer APD observed at the base compared to the apex. This was achieved by scaling the conductance of the slow delayed rectifier potassium current (G_{Ks}), based on findings by Szentadrassy et al. (2005), which reported significant differences in the expression levels of proteins forming the I_{Ks} channel between the apical and basal regions of the heart.

The anatomical model was segmented into the following three regions: apex, middle and base, each with a distinct scaling factor: 5 at the apex, 2.6 in the middle and 0.2 at the base, as described in Bueno-Palomeque et al. (2023a).

Figure 3 illustrates the APs incorporated in our biventricular model, across the three transmural layers (endocardial, midmyocardial and epicardial), while accounting for the different G_{Ks} values across the apicobasal regions. These repolarization heterogeneities were applied consistently to both the control \mathcal{C} (30-30-40) model and each of the globular \mathcal{G} (30-30-40) models.

In addition the impact of transmural repolarization variability on the analysed ECG biomarkers, particularly those related to repolarization, was assessed by reducing the width of the midmyocardial layer, the region with longer APD values. For this purpose, the control \mathcal{C} model and the globular \mathcal{G}_7 model, see 'Globular anatomical models' section, were configured with 48% of endocardium, 4% midmyocardium and 48% epicardium, denoted as \mathcal{C} (48-4-48) and \mathcal{G}_7 (48-4-48), respectively (Fig. 4). \mathcal{G}_7 model was selected due to its intermediate

profile in terms of variation in ventricular tissue volume (VTV).

Extracellular potentials were calculated at the positions of virtual electrodes using a torso model to generate a virtual 12-lead ECG, with the same sampling rate as in real recording, 1000 Hz. The onset, peak and endpoint of the virtual ECG waves were identified through their delineation on the transformed leads obtained by applying PCA to the eight independent virtual leads, following the same process described in 'ECG signal processing and the computation of biomarkers' section.

Globular anatomical models

The geometric changes resulting from IUGR were represented by constructing eight globular \mathcal{G} models. These models were developed departing from the control \mathcal{C} model, with a reduction of SpI and an increase in the width \mathcal{W} of the left ventricular wall.

The deformation was generated by displacing the nodes, $\mathbf{n}_k = [x_k \ y_k \ z_k]$, with nodal displacement leading to $\mathbf{d}_k = [u_k \ v_k \ w_k]$ to reach the new node location at $\mathbf{n}_k + \mathbf{d}_k$.

To modify ϕ from the value in the control geometry, we applied a tensile force along the radial direction of the transverse X, Y -axis plane. This led to a displacement $f_x(x_k)$ and $f_y(y_k)$ along the x_k and y_k coordinates, expressed as

$$\mathbf{d}_k = [f_x(x_k) \ f_y(y_k) \ 0],$$

$f_x(x_k)$ and $f_y(y_k)$ are set to 0 for x_k and y_k located on the right ventricular wall.

To reduce the \mathcal{L} length, another strategy was used. This displacement was expressed as

$$\mathbf{d}_k = [0 \ 0 \ f_z(z_k)].$$

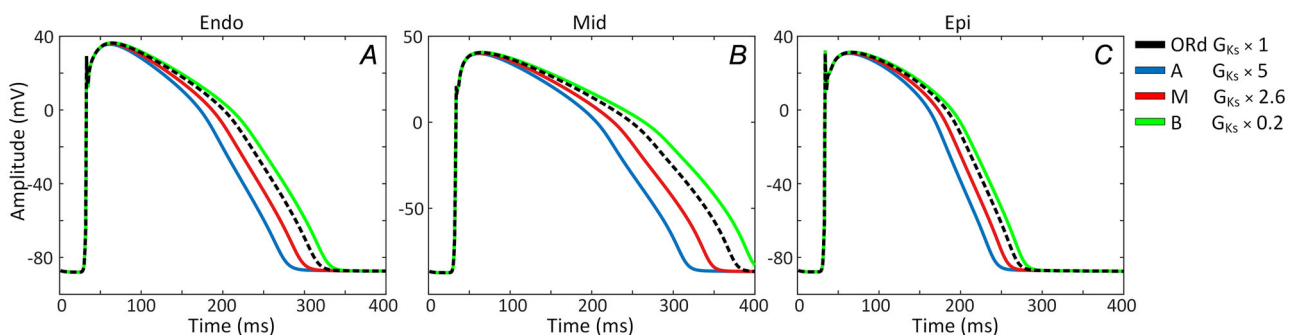


Figure 3. Simulated AP profiles implemented in the study

Action potential (AP) for cells incorporating both transmural (endo, mid and epi) and apicobasal (apex (A), middle (M) and base (B)) heterogeneities into the biventricular model.

In this case, a scaling factor α was introduced to homogeneously reduce the length \mathcal{L}_{AB} to $\mathcal{L}_{AB} - \Delta\mathcal{L}_{AB}$, where

$$\alpha = \frac{\Delta\mathcal{L}_{AB}}{\mathcal{L}_{AB}}. \quad (7)$$

The displacement along the longitudinal Z-axis was calculated as

$$f_z(z_k) = \alpha(z_r - z_k), \quad (8)$$

where z_r represents the zero displacement reference coordinate.

Geometrical models were re-meshed as in Zacur et al. (2017) to achieve the same target edge length (887 μ m). This was done by re-meshing the surface using an in-house implementation of the algorithm outlined in Botsch & Kobbelt (2004), resulting in a surface mesh of high quality, as expected from state-of-the-art techniques. The surface mesh was then used as input for Tetgen (Hang, 2015). The average edge length and quality of the mesh elements were assessed using VTK. Furthermore convergence tests indicated no significant variations in QRS_d .

The different geometric variations corresponding to each of these \mathcal{G}_i models are observed in Fig. 5. The variation in \mathcal{L} of the \mathcal{G}_i models relative to the \mathcal{C} model had a median value of 6.9 (4.6–9.6) mm, whereas ϕ showed a median value of 2.3 (0.4–2.6) mm. The globular models are organized considering \mathcal{W} , and their detailed descriptions are as follows:

- Model \mathcal{G}_1 was generated based on the percentage variation in ϕ and \mathcal{L} , derived from the average findings in Sarvari et al. (2017), with increases of 2.7% and reductions of 6.6%, respectively. This model has an 8.4% reduction in the left SpI and an increment of 2.3% in \mathcal{W} relative to the \mathcal{C} model.
- Model \mathcal{G}_2 : This globular model aimed to generate a more pronounced deformation, pushing the boundaries of variability as presented in Sarvari et al. (2017). The left SpI was reduced by 16%, with greater

expansion of ϕ and further reduction of \mathcal{L} compared to \mathcal{G}_1 . The increment in \mathcal{W} was 2.3% relative to the \mathcal{C} model.

- Model \mathcal{G}_3 : In this model, the left SpI was reduced by 14.8%, an increment of 7.1% in \mathcal{W} and 5% reduction in VTV compared to the \mathcal{C} model.
- Model \mathcal{G}_4 : In this model, \mathcal{W} increased by 7.3% compared to the \mathcal{C} model.
- Model \mathcal{G}_5 : The \mathcal{C} model was modified by applying surface traction to the epicardial tissue, increasing the left \mathcal{W} by approximately 4 mm (22.0% compared to \mathcal{C}). This increase led to a 9.9% increase in VTV compared to the \mathcal{C} model, with a corresponding reduction in left SpI of 10.9%.
- Model \mathcal{G}_6 : This model featured extreme thickening of \mathcal{W} (33.8% compared to \mathcal{C}) along with a reduced basal diameter ϕ . The left ϕ was reduced by 16% and \mathcal{L} by 21%. This produced a reduction of approximately 5% in the left SpI. This model drastically reduced the left ventricular cavity such that the total VTV of the model increased minimally by 0.04% compared to the \mathcal{C} model.
- Model \mathcal{G}_7 : This model displayed moderate changes. The left ϕ increased by 0.44% and \mathcal{L} was reduced by 8.6%. This resulted in a reduction of 8.5% in the left SpI. There was an increase in \mathcal{W} by 35.3% and VTV by 8.6%.
- Model \mathcal{G}_8 : This model exhibited an approximately 40% increase in muscular mass compared to the \mathcal{C} model. The left SpI was reduced by 14.4%. The \mathcal{W} by 40.7% and VTV increased by 35.89%.

The VTV can be seen as an aggregated surrogate of a global heart size change, fusing apex-base, basal diameter and wall modifications. To evaluate the impact of geometric changes on the depolarization and repolarization phases, the electrophysiological characteristics of the \mathcal{G}_i models, including fibre orientation, ventricular heterogeneities and conduction velocity, were kept as in the \mathcal{C} model. Only the Purkinje network was adjusted to adapt to the new dimensions of the endocardial surface of the \mathcal{G}_i models. Table 1 shows

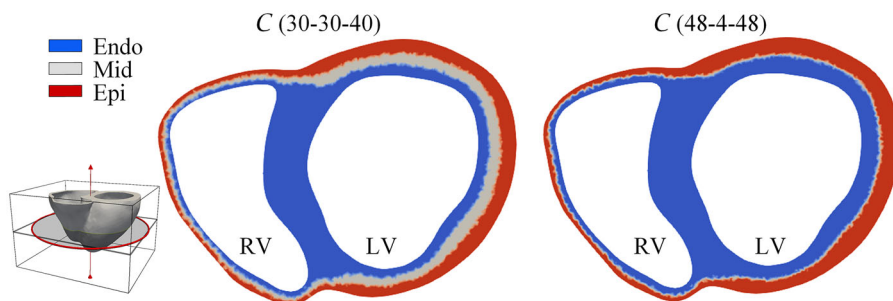


Figure 4. Reduction of the midmyocardial layer

Cross-sectional view of the control model $\mathcal{C}(30-30-40)$ with 30% endocardium, 30% mid-myocardium and 40% epicardium, and for $\mathcal{C}(48-4-48)$ model with its corresponding transmural distribution.

Table 1. Measurements of \mathcal{L} , ϕ , \mathcal{W} and ratio Spl in both ventricles for the \mathcal{C} and \mathcal{G} models. \mathcal{W} shows the maximum width of the left ventricle measured at the base of the biventricular model, and the last column shows the VTV of the entire ventricular mesh models

Model	Left ventricle				Right ventricle			VTV (cm ³)
	\mathcal{L} (mm)	ϕ (mm)	Spl	\mathcal{W} (mm)	\mathcal{L} (mm)	ϕ (mm)	Spl	
\mathcal{C}	69.5	45.8	1.5	13.1	57.3	42.4	1.4	139.8
\mathcal{G}_1	65.0	47.0	1.4	13.4	53.0	42.0	1.3	131.0
\mathcal{G}_2	61.1	48.2	1.3	13.4	51.1	41.1	1.2	125.3
\mathcal{G}_3	61.7	48.0	1.3	14.0	51.0	41.8	1.2	132.6
\mathcal{G}_4	64.9	48.5	1.3	14.0	53.3	41.5	1.3	131.0
\mathcal{G}_5	64.8	48.2	1.3	16.0	54.4	41.1	1.3	153.6
\mathcal{G}_6	54.9	38.3	1.4	17.5	48.1	42.7	1.1	139.8
\mathcal{G}_7	63.5	46.0	1.4	17.7	52.7	42.6	1.2	151.9
\mathcal{G}_8	59.4	46.0	1.3	18.4	49.3	42.6	1.2	189.9

the variations in basal diameter ϕ , apex-base length \mathcal{L} , wall thickness \mathcal{W} and VTV for the eight globular models \mathcal{G}_i with $i \in \{1, \dots, 8\}$, compared to the \mathcal{C} model.

All measurements for computing results were taken from the third simulated heartbeat. QRS complex measurements were performed on the PCA_{QRS} lead, whereas measurements of the T-wave were performed on the PCA_T lead. The association between the resulted values for QRS_d, T_{pe} and the QT interval and changes in \mathcal{L} , ϕ and \mathcal{W} was assessed using multiple linear regression.

Results

Clinical results from the preadolescent cohort

ECG biomarkers for the depolarization and repolarization phases were computed for the cohort of 93 pre-adolescent subjects, using the PCA_{QRS} and PCA_T leads. The results, presented in Table 2 a, include the median values and inter-quartile ranges (IQRs) of the measured biomarkers.

The comparison between the control and IUGR cohorts revealed differences in the ECG interval measurements.

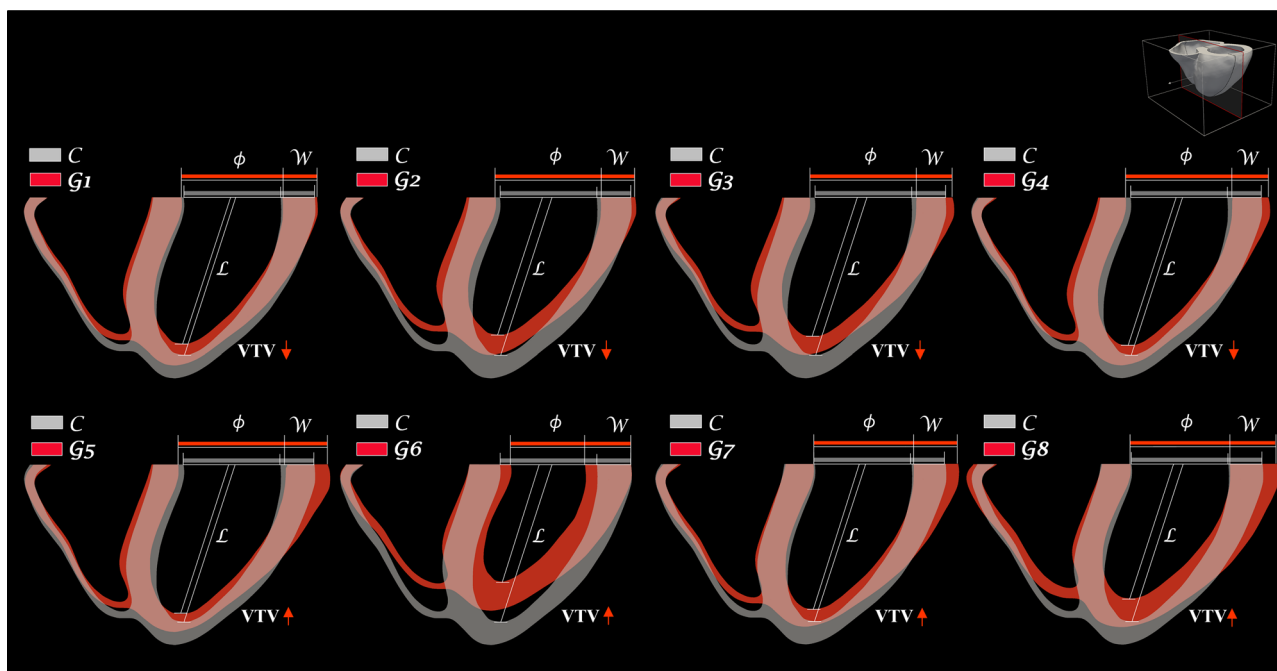


Figure 5. Eight \mathcal{G} models generated from \mathcal{C} model

The cross-section of the models allows for the observation of changes in \mathcal{L} , ϕ , Spl, \mathcal{W} and VTV. The direction of the arrows indicates the direction of change in the VTV parameter of the globular models compared to the control (an upward arrow indicates an increase).

Table 2. (a) ECG biomarkers from clinical data in preadolescents: control cohort ($n = 60$) and IUGR cohort ($n = 33$). (b) ECG biomarkers computed from simulations across the \mathcal{G}_i models. All simulations used $RR = 1$ s, so the QT and T_{pe} values are the same than their corrected counterparts, QT_c and $T_{pe,c}$, respectively.

Markers	ECG intervals (ms)				Waves amplitude (mV)	
(a) Clinical result in preadolescents, median (IQR)						
Dataset	QRS _d	T _{pe,c}	QT _c	T _{pe,c} /QT _c	QRS _a	T _a
Control	83(74–89)	76(74–81)	391(376–406)	0.196(0.188–0.207)	2.9(2.4-3.5)	0.8(0.6–1.0)
IUGR	87(81–90)	78(76–83)	389(381–399)	0.202(0.196–0.212)	3.1(2.3-3.6)	0.7(0.5–0.9)
p-value	0.039	0.031	0.703	0.026	0.553	0.318
(b) Computational simulations						
Model	QRS _d	T _{pe}	QT	T _{pe} /QT	QRS _a	T _a
C	64.0	76	340	0.223	1.86	1.21
G ₁	69.0	78	344	0.226	1.76	1.29
G ₂	69.5	77	341	0.225	1.69	1.33
G ₃	72.0	75	343	0.218	2.25	1.18
G ₄	71.5	76	344	0.220	2.18	1.18
G ₅	81.5	78	343	0.227	1.78	1.37
G ₆	67.0	78	341	0.228	2.31	1.33
G ₇	76.0	79	344	0.229	2.04	1.33
G ₈	75.0	79	345	0.229	2.13	1.31

In the depolarization-related properties, the IUGR cohort showed a significant median increase of 4 ms in QRS_d, with hardly any changes in QRS complex amplitude (QRS_a) compared to the control cohort. In the repolarization-related properties the IUGR cohort demonstrated a significant but moderate increase of 2 ms in median in T_{pe,c} and T_{pe,c}/QT_c ratio. Although the QT_c interval as well as the T-wave amplitude (T_a) were slightly lower in the IUGR cohort, these decreases were not statistically significant.

In Silico analysis of geometric effects on ECG biomarkers

The *in silico* study explored the impact of geometric changes associated with IUGR on depolarization and repolarization ECG biomarkers using the different globular electrophysiological models, all derived from the biventricular control \mathcal{C} model. As shown in Table 2 b, the simulations revealed significant changes in QRS_d along with more subtle changes in the T_{pe}, all of which align with the clinical findings listed in the top section.

QRS_d values, measured on PCA_{QRS} lead from the different models, as shown in Table 2 b and illustrated in Fig. 6A, reveal an increase relative to control \mathcal{C} , ranging from 3 ms in \mathcal{G}_6 to 17.5 ms in \mathcal{G}_5 .

Measurements of T_{pe} and QT intervals in the PCA_T lead, as illustrated in Fig. 6B, showed minor fluctuations, in line with clinical findings. The T_{pe} increased in six of the eight models, with a maximum increase of 3 ms in \mathcal{G}_7 and \mathcal{G}_8 . The QT interval increased across all models,

ranging from a 1-ms increase in \mathcal{G}_2 and \mathcal{G}_6 to a 5-ms increase in \mathcal{G}_8 . The increase in T_{pe} in the globular models is similar to that found in clinical measurements, with a median value of 2 ms. QT, on the contrary, shows a change in the opposite direction to the clinical results, with a median increase of 3.5 ms in the globular models. The T_{pe}/QT ratio increases in the globular models, in agreement with the clinical results.

The geometric changes in the globular models resulted in small changes in QRS_a, as shown in Table 2 b. The globular models exhibited an increase in QRS_a (median = 2.09 mV) compared to the control model, consistent with clinical findings. Conversely T_a in the globular models also showed an increase (median = 1.32 mV), which contrasts with the trends observed in clinical results.

Relationship between geometric variations and ECG biomarkers. Table 3 presents the results of the multiple linear regression analysis examining the relationship between the geometric properties { \mathcal{L} , ϕ and \mathcal{W} } and the biomarkers measured from the virtual ECG. Each of the ECG biomarkers was modelled as a linear combination of the three modified geometric parameters, which were treated as independent variables. This allowed us to assess both the extent to which anatomical variables account for changes in ECG biomarkers and the individual contribution of each anatomical variable to the ECG biomarker values.

The multiple regression analysis shows that anatomical variables contribute more significantly to QRS_d and,

to a lesser extent, to T_{pe} . In the regression model that considers individual variables, none of the three anatomical variables (\mathcal{L} , ϕ and \mathcal{W}) individually explain the variability in any of the markers, except for the contribution of \mathcal{W} to T_{pe} with a regression coefficient $\mathcal{B} = 0.50$ and p -value = 0.019.

When combining the independent geometric variables in pairs, the combination of ϕ and \mathcal{W} significantly contributes to QRS_d ($\mathcal{B} = 1.40$ and 2.22 , with p -values = 0.010 and 0.007, respectively). For T_{pe} , in the same combination, \mathcal{W} shows a significant value ($\mathcal{B} = 0.52$, p -value = 0.044). In the same ECG biomarker, but in the combination of \mathcal{L} and \mathcal{W} , the latter shows a significant value ($\mathcal{B} = 0.57$, p -value = 0.039).

Combining all three variables together the anatomical variables have a strong contribution to QRS_d , accounting for 77% of its variance. \mathcal{B} value revealed that increases in both basal diameter ϕ ($\mathcal{B} = 1.43$, p -value = 0.028) and left ventricular wall thickness \mathcal{W} ($\mathcal{B} = 2.18$, p -value = 0.023) lead to an increase in QRS_d . In contrast, the apex-to-base length \mathcal{L} has a minimal impact on QRS_d .

Unlike QRS_d , the T_{pe} and QT intervals exhibited a moderate correlation with the anatomical parameters ($R^2 = 0.59$ and 0.57 , respectively), with the increase in wall thickness \mathcal{W} being the most significant anatomical factor

contributing to the enhancement of these repolarization features ($\mathcal{B} = 0.57$ and 0.58 , respectively).

Role of transmural heterogeneities. The impact of electrophysiological transmural heterogeneities on the findings of this study was evaluated by reducing the mid-myocardial layer (which has the longest APD values), thereby increasing the endocardial and epicardial layers in \mathcal{C} and \mathcal{G}_7 .

Changes in transmural heterogeneities did not affect QRS_d in either the control (64 ms) or globular heart models (76 ms), as shown in Table 4. This lack of impact is because removing the midmyocardial layer mainly affects the APD within the transmural wall, affecting the repolarization phase rather than the depolarization phase, which defines QRS_d .

Therefore transmural heterogeneities show an impact on the repolarization T_{pe} and QT intervals. The removal of the midmyocardial layer resulted in a moderate reduction of the T_{pe} , with a decrease of 1 ms in the control models and a 3-ms reduction in the globular model \mathcal{G}_7 . A reduction in the QT interval is observed, with a decrease of 11 ms in the control models and 13 ms in the globular models. This reduction occurs because the removal of the midmyocardial layer enlarges the end-

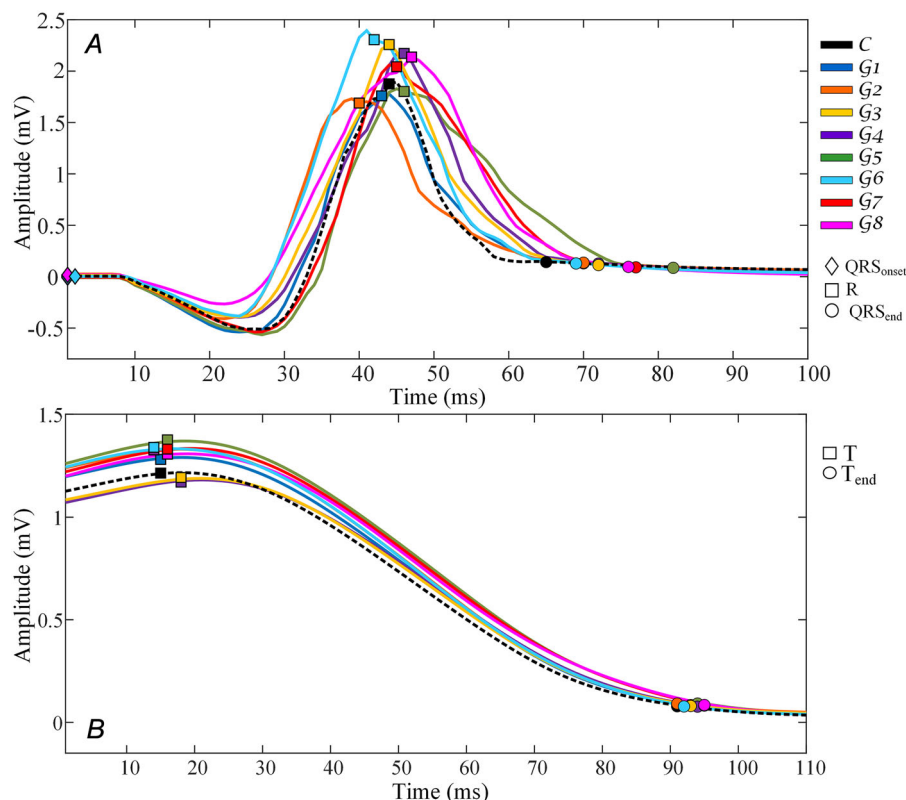


Figure 6. Measurement of intervals on the virtual ECG

(A) QRS complex in lead PCA_{QRS} of the \mathcal{C} model and \mathcal{G}_i models, with the marks of the QRS_{onset} , QRS_{peak} and the QRS_{end} . (B) T_{pe} in PCA_T lead of the \mathcal{C} and \mathcal{G}_i models with the marks of the T_{peak} , and the T_{end} .

Table 3. Multiple regression analysis between the geometric variables of globular models (\mathcal{L} , ϕ and \mathcal{W}) and the QRS_d, T_{pe} and QT intervals measured in the virtual ECG. p_i indicates the p -value for each individual variable, whereas p_F represents the significance value of the model. Values with p -value < 0.05 are highlighted in bold.

Marker	QRS _d				T _{pe}				QT			
	β	p_i	R^2	p_F	β	p_i	R^2	p_F	β	p_i	R^2	p_F
Individual variables												
\mathcal{L}	−0.04	0.930	0.001		−0.11	0.382	0.11		−0.02	0.901	0.002	
ϕ	0.65	0.297	0.15		−0.14	0.400	0.10		0.19	0.344	0.13	
\mathcal{W}	1.19	0.188	0.23		0.50	0.019	0.57		0.32	0.297	0.15	
Pairs combined variables												
\mathcal{L}	−0.58	0.339	0.28	0.370	−0.07	0.673	0.13	0.655	−0.19	0.360	0.25	0.421
ϕ	1.13	0.176			−0.08	0.718			0.35	0.208		
\mathcal{L}	0.50	0.380	0.33	0.297	0.06	0.601	0.59	0.071	0.12	0.550	0.21	0.500
\mathcal{W}	1.76	0.135			0.57	0.039			0.45	0.261		
ϕ	1.40	0.010	0.77	0.013	0.03	0.819	0.57	0.080	0.40	0.055	0.56	0.084
\mathcal{W}	2.22	0.007			0.52	0.044			0.61	0.050		
All three variables together												
\mathcal{L}	−0.06	0.885	0.77	0.048	0.06	0.670	0.59	0.188	−0.05	0.794	0.57	0.206
ϕ	1.43	0.028			0.00	0.987			0.43	0.095		
\mathcal{W}	2.18	0.023			0.57	0.066			0.58	0.113		

Table 4. Intervals and amplitudes measured on the control \mathcal{C} and globular \mathcal{G}_7 models with different transmural divisions: 30, 30 and 40% for endocardium, mid-myocardium and epicardium, and 48, 4 and 48%, respectively

Model marker	ECG intervals (ms)				Amplitude (mV)	
	QRS _d	T _{pe}	QT	T _{pe} /QT	QRS _a	T _a
\mathcal{C} (30-30-40)	64	76	340	0.223	1.86	1.21
\mathcal{C} (48-4-48)	64	75	329	0.227	1.86	1.21
\mathcal{G}_7 (30-30-40)	76	79	344	0.229	2.04	1.33
\mathcal{G}_7 (48-4-48)	76	76	331	0.229	2.03	1.27

ocardial and epicardial regions, both of which exhibit shorter and more comparable APDs, leading to reduced repolarization dispersion and, consequently, shorter T_{pe} and QT intervals.

No significant effect of the midmyocardial reduction is observed on the T_{pe}/QT or the maximum amplitudes QRS_a and T_a.

Mechanisms behind the subtle T_{pe} changes compared to the larger QRS_d changes. To gain a deeper insight into the subtle changes in the T_{pe} compared to the significant change in QRS_d, we analysed the AP at three node positions spanning from the endocardium to the epicardium across all globular models. These three nodes are transmurally distributed in all models: one is located at the centre of the endocardial-base section (P1_{endo}), another at the centre of the epicardial-base section (P2_{epi}) and the third on the external epicardial-base surface of the left ventricle (P3_{epi-e}), which corresponds to the last region to depolarize.

To analyse the changes in the QRS complex, we examined the differences in activation time (AT) at each node across the different globular models, which represent the onset of depolarization. These ATs correspond to the APD at 90% repolarization (APD₉₀), a key metric that defines the APD. Figure 7A shows that the epicardial surface (P3_{epi-e}) consistently defines the end of activation (i.e. the region with the most delayed or longest AT) across all anatomical models. Note that across the different P3_{epi-e} nodes, the AT values vary between 54 and 65 ms, corresponding to the phase between the R and S waves of the QRS complex in Fig. 6, marking the end of activation. In addition, beyond the impact of changes in \mathcal{L} and ϕ , we found that the thicker the ventricular wall, the longer it takes for P3_{epi-e} to activate (highlighted by the magenta circle, which represents the model with the greatest wall thickness).

At P1_{endo}, AT values in the \mathcal{G}_i models shows low variability, averaging 35.6 ± 1.6 ms, close to the \mathcal{C} model's 35 ms. In contrast, at P2_{epi}, AT increases to 54.8 ± 4.6 ms and at P3_{epi-e}, it reaches 58.6 ± 5.42 ms. Several

globular models display a delayed AT relative to the \mathcal{C} model.

The \mathcal{G}_i models showed an average APD₉₀ of 299.6 ± 2.56 ms at P1_{endo}, 247.5 ± 4.5 ms at P2_{epi} and 235.3 ± 4.5 ms at P3_{epi-e} (see Fig. 7A). At P1_{endo}, most \mathcal{G}_i models exceed the APD₉₀ of the \mathcal{C} model; however, this pattern reverses in the epi nodes, where APD₉₀ is shorter. This is attributed to the wider epicardial layer, which reduces the influence of the adjacent midmyocardium's longer APD₉₀ at the surface P3_{epi-e}. These differences may explain why the QT biomarker remains unchanged despite the significant widening of QRS_d.

Figure 7B illustrates the repolarization time (RT) of each node across all models, calculated as the sum of AT and APD₉₀, expressed as $RT = AT + APD_{90}$. The figure indicates that the endocardium is the last region to repolarize for all models, implying that the end of the T-wave is determined by the APD characteristics of the endocardium. Therefore wall thickness has minimal impact on the end of the T-wave and consequently has little effect on the T_{pe} or QT intervals.

To visualize the variation in AT between the control model and the globular models, Fig. 8 was included, with an emphasis on the ventricular base. The AT maps in all \mathcal{G}_i models, except for \mathcal{G}_4 , indicate that AP propagation to the base of the left ventricle occurs more rapidly compared to the \mathcal{C} model, particularly in the region around the endocardial surface of the left ventricle. The faster propagation is attributed to the reduction of \mathcal{L} in all \mathcal{G}_i models, which, in turn, shortens the AP propagation time. The \mathcal{G}_i models with greater increases in \mathcal{W} show their impact on a longer AT on the outer epicardial surface of the left ventricle. The greatest AT delay is observed in

models \mathcal{G}_5 and \mathcal{G}_8 , where VTV is larger compared to the other globular models.

In Fig. 9, the calculated ECGs for each of the eight virtual leads, along with the PCA_{QRS} and PCA_T leads, are shown. In all leads, the globular models show an earlier depolarization phase (earlier red upstroke of QRS complex), although minimal, due to the shortening of SpI. In addition, both QRS_d and QRS_a (specifically in precordial lead V6 and limb leads I and II) increase due to the thickening of the free ventricular wall.

T_a tends to increase in the globular models, and in the PCA_T measurements, all \mathcal{G}_i models exhibit an amplitude increase, except for \mathcal{G}_3 and \mathcal{G}_4 . Regarding the end of the T-wave, hardly differences are observed between the \mathcal{G}_i models and the control model \mathcal{C} .

Discussion

Electrophysiological variations associated with IUGR have been identified in different age cohorts (Bueno-Palomeque et al., 2023a, 2023b; Ortigosa et al., 2016) and linked to cardiovascular complications (Schirone et al., 2017; Visentin et al., 2014). Understanding the impact of reduced left ventricular SpI, increased \mathcal{W} and VTV on cardiac electrical activity could contribute to a better understanding of IUGR-related cardiac re-modelling. This study reports the changes in depolarization and repolarization intervals in control and IUGR subjects. The results from the analysis of clinical data support that the geometric changes associated with IUGR appeared together with an electrophysiological alteration, which could be hypothesized to be related, at

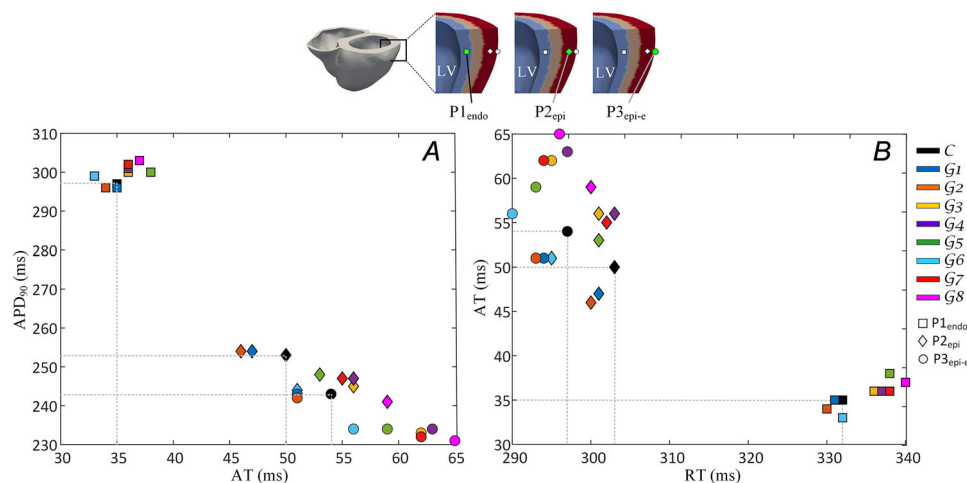


Figure 7. Activation time (AT), repolarization time (RT), and action potential duration (APD) at three nodes of the mesh

(A) Activation time (AT) and action potential durations (APD) at three nodes of the mesh, P1_{endo} on an intermediate node of the endo-base section, P2_{ep} on the middle epi-base section and P3_{ep-e} on the external surface of the epi-base section (B) A contrast between RT and AT is presented, considering the three selected nodes. The upper part of the figure outlines the location of these nodes within the heart volume.

least partially. In addition, this study simulates anatomical cardiac changes due to IUGR using eight different \mathcal{G}_i models, derived from a control \mathcal{C} model, to assess their impact on depolarization and repolarization ECG intervals, using computational models based on a realistic heart and torso anatomy.

The IUGR cohort presented a significantly prolonged QRS_d compared to the control cohort (Table 2). This increase could be associated with a greater ventricular wall thickness \mathcal{W} , which delays electrical propagation, widening the QRS complex. The significant increase in T_{pe,c} could also be linked to the thickening of the left \mathcal{W} . However the QT_c interval was found to be not significantly reduced in the IUGR cohort.

Regarding the change in QRS_d our results align with previous studies (Grimm et al., 2003; Van Leeuwen et al., 2001), where its prolongation and a greater QT dispersion were also observed in Velayo et al. (2017). We hypothesize that the increase in \mathcal{W} impacts the intervals, especially T_{pe}. To analyse the influence of geometric re-modelling on electrophysiology, *in silico* tests were conducted to better understand this relationship.

Cardiac re-modelling *in silico*

Cardiac re-modelling was simulated by deforming the \mathcal{C} model into more globular ones \mathcal{G}_i with $i \in \{1, \dots, 8\}$. Magnitude of changes in ϕ and \mathcal{L} was based on geometric changes observed in clinical data, with the \mathcal{G}_1

model aiming for a percentage change similar to that reported in Sarvari et al. (2017), with subsequent models incrementally increasing these changes to evaluate their electrophysiological impact. Deformations focused on the left ventricle, but geometric effects also affected the right ventricle. \mathcal{L} changes in the left ventricle affected the entire model, leading to an average reduction of 9.4% in right ventricular \mathcal{L} , with a median value of 51.9 (50.5–53.0) mm. The right ventricular ϕ decreased by 1.2%, to 41.9 (41.4–42.6) mm, and the right ventricular SpI decreased by 8.15%.

The left ventricular \mathcal{W} increased, primarily at the base, except in \mathcal{G}_8 , where it increased by approximately 40% in both ventricular walls and in \mathcal{G}_6 , increasing the width of the left ventricle inward (see \mathcal{G}_8 and \mathcal{G}_6 in Fig. 5). VTV increases, as shown in Table 1, mainly as a reflection of the increase in left ventricular wall width \mathcal{W} . This width increase is significant in IUGR infants (Cruz-Lemini et al., 2014) and noticeable, though non-significantly, in pre-adolescents (Sarvari et al., 2017).

The Purkinje network applied to the \mathcal{G}_i models was reduced in length in the apex-base direction and widened in the diametrical ϕ direction compared to the \mathcal{C} model. Its effect on an earlier activation is evident when observing the AT on the epicardial periphery of the left ventricle in Fig. 9 for all \mathcal{G}_i models. Although this reduction in the \mathcal{L} direction brought nodes closer, generating areas with a higher node density, no evidence was found of conduction system changes due to IUGR. This study focused on

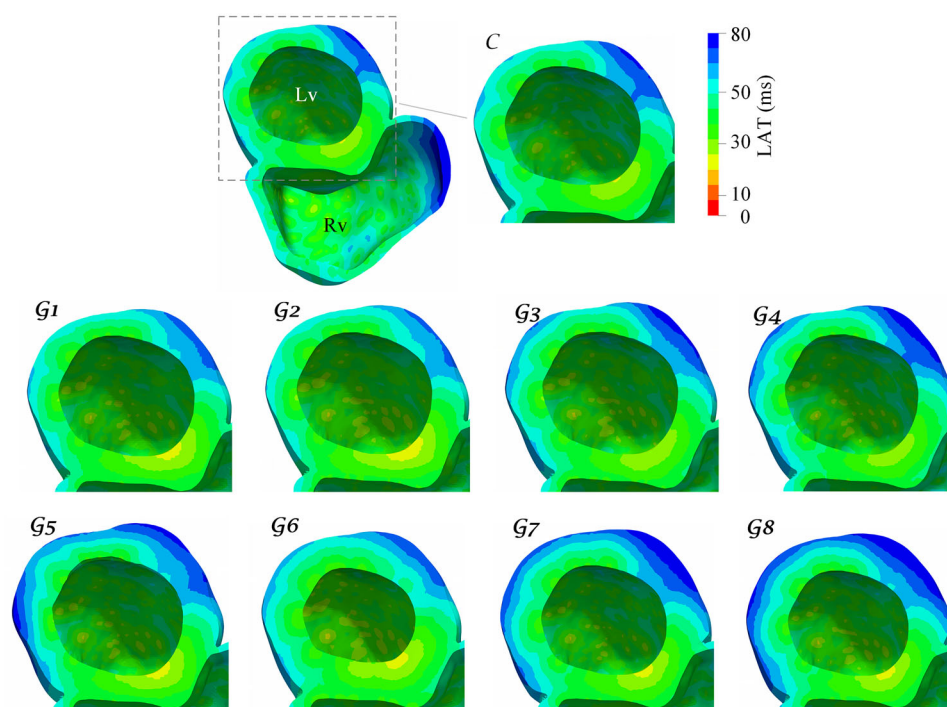


Figure 8. Activation time (AT) maps on the left ventricle of each globular model

The control model is displayed at the top.

the geometric changes; hence the same Purkinje network configuration was used throughout the models.

For the simulated ECG on virtual electrodes, considering the QRS complex, almost all models exhibited increased QRS_d across all leads, also visible in QRS_d measurements on PCA_{QRS} . A slight increase in QRS_a and T_a is also evident. In \mathcal{G}_8 , the model with the highest VTV increase, a significant rise in T_a is observed, mainly in leads V2, V3 and V4 (see Fig. 9).

The geometric changes applied to the globular models in this study were implemented as linear variations from base to apex across the ventricular wall. Although alternative strategies could have been considered, we opted for gradual changes, as no evidence supporting non-homogeneous changes was found (Sarvari et al., 2017).

Impact of left basal diameter ϕ and wall width \mathcal{W} in QRS_d . Previous studies have reported that during the fetal stage, changes in QRS_d exhibit contradictory patterns, as we can see in Brambati & Bonsignore (1982), Pardi & Marconi (1986) and Smith et al. (2019). However, in our study, with an IUGR and control preadolescent cohort, a significant median QRS_d increase of 4 ms (p -value = 0.039) was observed (see Table 2 a).

In addition to these findings, we found in simulation that all globularly deformed \mathcal{G}_i models showed an increase in QRS_d , compatible with our clinical results and those pointing to QRS_d widening as a result of IUGR conditioning. Through multiple regression analysis, it is observed that in QRS_d , a significant contribution of its variance depends on geometric changes with an $R^2 = 0.77$ and p -value = 0.048. Two of the parameters alone have

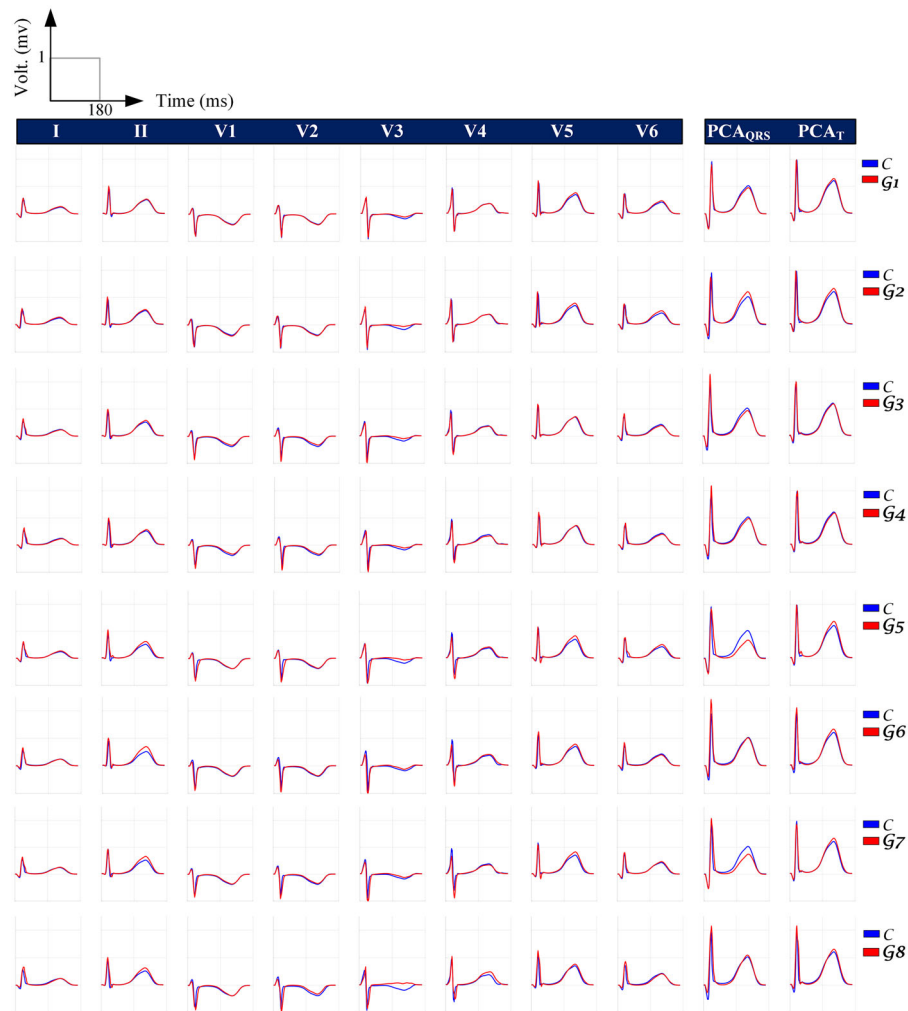


Figure 9. Eight independent standard electrocardiogram (ECG) leads, together with PCA_{QRS} , and PCA_T leads for each \mathcal{G}_i model, overprinted with the ECGs from \mathcal{C} model. The third beat of each simulation was represented.

a p -value < 0.05 (ϕ : p -value = 0.028 and \mathcal{W} : p -value = 0.023), indicating that these variables have a significant impact on the change in QRS_d . These values should be analysed with caution due to the limited number of simulations (eight cases).

The deformations in wall ventricular thickness \mathcal{W} varied across the models and revealed a strong relationship between the increase in \mathcal{W} at the base and the rise in QRS_d . For instance \mathcal{G}_6 produces the smallest change in QRS_d (3 ms) and exhibits an increase in \mathcal{W} towards the interior of the ventricle. In contrast model \mathcal{G}_5 shows an increase in \mathcal{W} in the opposite direction, with a corresponding QRS_d increase of 17.5 ms.

In middle-aged and older adults, a $\text{QRS}_d > 100$ ms significantly increases heart failure risk (Ilkhanoff et al., 2012). In this study in both clinical results ($\text{QRS}_d = 87$ (81–90) ms and *in silico* results, QRS_d did not exceed 81.5 ms, even in the extreme case of \mathcal{G}_5 , probably indicating either a low cardiac risk for their age, a not fully developed heart, or both, but pointing to higher propensity in the IUGR cases. Clinical data showed an increase in QRS complex maximum amplitude in the IUGR cohort, replicated in the models (\mathcal{G}_3 , \mathcal{G}_4 , \mathcal{G}_6 to \mathcal{G}_8) simulations.

The VTV feature as such does not capture well the morphological changes induced by IUGR. Note that only three out of eight cases (\mathcal{G}_5 , \mathcal{G}_7 and \mathcal{G}_8 , see Table 1), result in larger VTV than the control heart \mathcal{C} . When computing the regression of the ECG parameters QRS_d , T_{pe} and QT with VTV, no significant correlation in any case was found, implying that the translation of VTV to ECG changes is not straightforward. On the contrary we observed that morphological features, such as basal enlargement or apex-base length, correlated to the observed changes in ECG characteristics.

T_{pe} and QT intervals. The T_{pe} , related to spatial dispersion of ventricular repolarization, is significantly increased with hypertrophy (Mozos & Serban, 2011). Clinical results showed a significant heart rate corrected T_{pe} , $T_{pe,c}$, increase of 2 ms in the IUGR cohort (p -value = 0.031) and a non-significant decrease in T-wave amplitude of 0.15 mV. In simulations, Table 2 b shows a small T_{pe} increase, with a maximum change of 2 ms. Except for \mathcal{G}_3 and \mathcal{G}_4 , T_{pe} increased in all globular models. The reduction here seems to be related to T-wave peak delay associated with the lower T-wave amplitude (Fig. 6B).

The increase in VTV leads to a subtle rise in T_{pe} across all \mathcal{G}_i models, except for \mathcal{G}_3 and \mathcal{G}_4 . However the extreme increase in VTV in \mathcal{G}_8 does not result in a proportional rise in T_{pe} . In Table 3, we see that geometric changes do not have a significant effect on T_{pe} and QT.

The QT interval showed a non-significant reduction of 2 ms in median in clinical data. Despite the QRS_d increase the T_{end} mark remained nearly constant (Fig. 6B).

This is significant as the \mathcal{G}_i models underwent various geometric and volumetric changes without much effect on repolarization. The subtle differences in the QT interval indicate that the increase in \mathcal{W} does not significantly affect the repolarization phase. As shown in Fig. 7, the APD_{90} in epicardial cells shows that the delay in the depolarization phase does not directly affect the T_{end} point. In the same epi cells it is observed that the wider the \mathcal{W} in the left ventricle, the shorter the APD_{90} . In addition it can be seen that the endo cells determine the duration of QRS_d . Although endo cells activate earlier, they are the last to repolarize (Fig. 7B), which explains why QT does not show changes as remarkable as those observed in QRS_d .

Several methodologies exist for detecting and delineating ECG waves, potentially leading to different ECG interval values. However to ensure a meaningful comparative analysis of results across different models and between clinical and simulated data, it is essential to use the same algorithms, as has been done in this study, along with a reliable and widely used methodology (Martínez et al., 2004).

The reduction of the midmyocardial section had a direct impact on the T-wave, leading to a decrease in both the T_{pe} and QT intervals (see Table 4). However this effect occurs alongside changes induced by SpI and \mathcal{W} , which moderate the overall variation in these intervals. As expected, modifications in transmural composition did not influence QRS_d , aligning with previous findings (Bueno-Palomeque et al., 2023a). In addition, it is important to acknowledge the ongoing debate regarding the presence of M-cells with prolonged repolarization in human hearts. Interestingly when the midmyocardial layer is reduced, the differences in QT and T_{pe} intervals between the control and globular models become smaller, showing better agreement with the clinical results in Table 2.

A comparison of ECG wave intervals between the simulated models and clinical data reveals interesting differences in the order of magnitude, as shown in Table 2. Although the simulated QRS_d and T_{pe} parameters align well within clinical ranges, the QT interval exhibits a slightly higher deviation. This discrepancy may stem from differences in the RR interval or ionic properties between the control \mathcal{C} model design (Martínez-Navarro et al., 2019) and the average subject geometry in the dataset. However, as the primary analysis focuses on the relative changes between the globular and control models, this difference is not expected to significantly impact the comparative assessment.

All simulations were performed with $\text{RR} = 1000$ ms. This allows comparisons with repolarization intervals in ECGs recorded at different heart rates by considering heart rate corrected intervals, as presented in Table 2. Running simulations at different RR interval values could allow for more personalized heart rate analyses by

selecting ECG data from patients with matching RR intervals. However this would require a significantly larger dataset, which is beyond the scope of the current study.

The results suggest that the considered cardiac re-modelling primarily affects the depolarization cycle, notably QRS_d. The incorporated globular model changes only consider geometric variations. It can be speculated if other re-modelling, as conduction abnormalities or electrophysiological modifications, can add to better reproduce the ECG clinical observations. This can be the subject of future studies.

The main finding of this study underscores the effect of anatomical remodelling in IUGR-born subjects on the ECG, specifically prolonging the QRS_d without influencing the QT interval. The computational framework offers insights into the underlying mechanisms, identifying ventricular wall thickening at the base as the primary factor driving these effects, without any ionic re-modelling involved. It also represents a potentially useful clinical tool to monitor cardiac risk derived from the IUGR condition.

Limitations

Beyond its findings this study has some limitations that should be addressed. First the number of subjects in both the control and IUGR groups is limited. Although significant differences were identified in QRS_d and T_{pe}, the findings should be interpreted with caution. However the results provide a foundation for future research involving a larger cohort, which could further validate and refine the observed associations.

From a computational perspective this study has developed a simulation framework designed to achieve a realistic scenario, specifically analysing the effects of geometric changes resulting from IUGR while maintaining other parameters, such as the conduction system and propagation velocity, as constants. To achieve this, eight globular models were developed based on clinically observed geometric changes, incorporating additional modifications to evaluate their impact on cardiac electrophysiology. Although various alternative approaches could be explored for constructing globular models, the ones used in this study encompass a meaningful range of variations in ϕ , \mathcal{L} , \mathcal{W} and VTV. The findings highlight a strong relationship between changes in \mathcal{W} and their impact on QRS_d. Nevertheless, further investigation is necessary, considering parameters beyond those addressed in this study.

The selection of eight models represents a balance between comprehensive evaluation and capturing the range of plausible anatomical dynamics. Although a more extensive set of models with gradual variations could

provide deeper insights, this study offers valuable learning that can guide future work. Further refinements, including additional re-modelling, may help address phenomena not fully observed or replicated in this study.

Conclusion

This study has shown a direct relationship between anatomical cardiac remodelling and electrocardiographic (ECG) changes in a cohort of preadolescents born with IUGR. A significant increase in QRS complex duration (QRS_d) and a slight increase in the corrected T-peak-to-end (T_{pe,c}) interval were observed in ECG data when compared to the control cohort. However no significant differences were found in the QT interval.

In silico simulation results reveal that anatomical changes induced by IUGR, particularly in apex-base length, basal diameter and ventricular wall thickness, significantly impact electrocardiographic parameters. The observed increases in QRS_d and T_{pe} align with clinical data, reinforcing a direct connection between geometrical deformations and ECG modifications. However, although the simulated QT interval shows an average increase of ~1%, clinical observations show no change in the QT interval. This discrepancy may be attributed to cellular coupling within the computational mesh, affecting AP propagation during the T-wave, as evidenced by the pilot test generating a model with different transmural cellular distribution.

The variation in QRS_d in IUGR patients highlights a direct relationship with increased ventricular wall thickness, particularly at the basal region. In contrast, changes in T_{pe} and the QT interval, which are more strongly linked to transmural heterogeneities, highlight the need for further research to investigate additional electrophysiological mechanisms beyond the geometrical factors explored in this study.

References

- Aeschbacher, S., O'Neal, W. T., Krisai, P., Loehr, L., Chen, L. Y., Alonso, A., Soliman, E. Z., & Conen, D. (2018). Relationship between QRS complex duration and incident atrial fibrillation. *International Journal of Cardiology*, **266**, 84–88.
- Arnott, C., Skilton, M. R., Ruohonen, S., Juonala, M., Viikari, J. S. A., Kähönen, M., Lehtimäki, T., Laitinen, T., Celermajer, D. S., & Raitakari, O. T. (2015). Subtle increases in heart size persist into adulthood in growth restricted babies: The cardiovascular risk in young finns study. *Open Heart*, **2**, e000265.
- Barker, D. J. (1990). The fetal and infant origins of adult disease. *BMJ: British Medical Journal*, **301**, 1111.

- Bjarnegård, N., Morsing, E., Cinthio, M., Länne, T., & Brodzski, J. (2013). Cardiovascular function in adulthood following intrauterine growth restriction with abnormal fetal blood flow. *Ultrasound in Obstetrics and Gynecology*, **41**, 177–184.
- Botsch, M., & Kobbelt, L. (2004). A remeshing approach to multiresolution modeling. In *Proceedings of the 2004 Eurographics/ACM SIGGRAPH symposium on Geometry processing* (pp. 185–192).
- Brambati, B., & Bonsignore, L. (1982). Intraventricular conduction time in fetuses born with growth retardation. *British Journal of Obstetrics and Gynaecology*, **89**, 900–903.
- Bueno-Palomeque, F. L., Mountris, K. A., Mincholé, A., Ortigosa, N., Bailón, R., Pueyo, E., & Laguna, P. (2020, September). Changes in QRS and T-wave loops subsequent to an increase in left ventricle globularity as in intrauterine growth restriction: A simulation study. In *Computing in cardiology*.
- Bueno-Palomeque, F. L., Mountris, K. A., Ortigosa, N., Bailón, R., Bijmens, B., Crispi, F., Pueyo, E., Mincholé, A., & Laguna, P. (2023a). QRS-T angles as markers for heart sphericity in subjects with intrauterine growth restriction: A simulation study. *Institute of Electrical and Electronics Engineers Journal of Biomedical and Health Informatics*, **27**, 4707–4718.
- Bueno-Palomeque, F. L., Mountris, K. A., Ortigosa, N., Bailón, R., Bijmens, B., Crispi, F., Pueyo, E., Mincholé, A., & Laguna, P. (2023b). QRS width and T-peak to T-end interval are prolonged in preadolescents with severe intrauterine growth restriction at birth when compared to controls. In *Computing in cardiology* (Vol. 50).
- Castells, F., Laguna, P., Sörnmo, L., Bollmann, A., Roig, J. M., Roig, M., & Leif, S. (2007). Principal component analysis in ECG signal processing. *EURASIP Journal on Advances in Signal Processing* 2007, 1–21.
- Costabal, F. S., Hurtado, D. E., & Kuhl, E. (2016). Generating Purkinje networks in the human heart HHS public access. *Journal of Biomechanics*, **49**, 2455–2465.
- Crispi, F., Bijmens, B., Figueras, F., Bartrons, J., Eixarch, E., Noble, F.L., Ahmed, A., & Gratacós, E. (2010). Fetal growth restriction results in remodeled and less efficient hearts in children. *Circulation*, **121**, 2427–2436.
- Crispi, F., Sepúlveda-Martínez, A., Crovetto, F., Gómez, O., Bijmens, B., & Gratacós, E. (2020). Main patterns of fetal cardiac remodeling. *Fetal Diagnosis and Therapy*, **47**, 337–344.
- Cruz-Lemini, M., Crispi, F., Valenzuela-Alcaraz, B., Figueras, F., Sitges, M., Bijmens, B. & Gratacós, E. (2016). Fetal cardiovascular remodeling persists at 6 months in infants with intrauterine growth restriction. *Ultrasound in Obstetrics and Gynecology*, **48**, 349–356.
- Cruz-Lemini, M., Crispi, F., Valenzuela-Alcaraz, B., Figueras, F., Gómez, O., Sitges, M., Bijmens, B. & Gratacós, E. (2014). A fetal cardiovascular score to predict infant hypertension and arterial remodeling in intrauterine growth restriction. *American Journal of Obstetrics and Gynecology*, **210**, 552.e1–552.e22.
- De Onis, M., Blössner, M., & Villar, J. (1998). Levels and patterns of intrauterine growth retardation in developing countries. *European Journal of Clinical Nutrition*, **52**, S5–S15.
- Doste, R., Soto-Iglesias, D., Bernardino, G., Alcaine, A., Sebastian, R., Giffard-Roisin, S., Sermesant, M., Berrueto, A., Sanchez-Quintana, D., & Camara, O. (2019). A rule-based method to model myocardial fiber orientation in cardiac biventricular geometries with outflow tracts. *International Journal for Numerical Methods in Biomedical Engineering*, **35**(4), e3185.
- Dutta, S., Chang, K. C., Beattie, K. A., Sheng, J., Tran, P. N., Wu, W. W., Wu, M., Strauss, D.G., Colatsky, T., & Li, Z. (2017). Optimization of an in silico cardiac cell model for proarrhythmia risk assessment. *Frontiers in Physiology*, **8**, 616.
- Emori, T., & Antzelevitch, C. (2001). Cellular basis for complex T waves and arrhythmic activity following combined IKr and IKs block. *Journal of Cardiovascular Electrophysiology*, **12**, 1369–1378.
- Figueras, F., Meler, E., Iraola, A., Eixarch, E., Coll, O., Figueras, J., Francis, A., Gratacós, E. & Gardosi, J. (2008). Customized birthweight standards for a Spanish population. *European Journal of Obstetrics & Gynecology and Reproductive Biology*, **136**, 20–24.
- Fouzas, S., Karatza, A. A., Davlouros, P. A., Chrysis, D., Alexopoulos, D., Mantagos, S., & Dimitriou, G. (2014). Heterogeneity of ventricular repolarization in newborns with intrauterine growth restriction. *Early Human Development*, **90**, 857–862.
- Gima, K., & Rudy, Y. (2002). Ionic current basis of electrocardiographic waveforms: A model study. *Circulation Research*, **90**, 889–896.
- Grimm, B., Kaehler, C., Schleussner, E., Schneider, U., Haeisen, J., & Seewald, H.J. (2003). Influence of intra-uterine growth restriction on cardiac time intervals evaluated by fetal magnetocardiography. *Early Human Development*, **74**, 1–11.
- Gupta, P., Patel, C., Patel, H., Narayanaswamy, S., Malhotra, B., Green, J. T., & Yan, G. X. (2008). Tp-e/QT ratio as an index of arrhythmogenesis. *Journal of Electrocardiology*, **41**, 567–574.
- Hang, S. (2015). TetGen, a Delaunay-based quality tetrahedral mesh generator. *Association for Computing Machinery Transactions on Mathematical Software*, **41**(2), 11.
- Ilkhanoff, L., Liu, K., Ning, H., Nazarian, S., Bluemke, D.A., Soliman, E. Z., & Lloyd-Jones, D. M. (2012). Association of QRS duration with left ventricular structure and function and risk of heart failure in middle-aged and older adults: The Multi-Ethnic Study of Atherosclerosis (MESA). *European Journal of Heart Failure*, **14**, 1285–1292.
- Kléber, A. G., Janse, M. J., & Fast, V. G. (2011). Normal and abnormal conduction in the heart. In *Comprehensive physiology* (pp. 455–530). American Physiological Society.
- Martínez-Navarro, H., Mincholé, A., Bueno-Orovio, A., & Rodríguez, B. (2019). High arrhythmic risk in antero-septal acute myocardial ischemia is explained by increased transmural reentry occurrence. *Scientific Reports*, **9**, 16803.
- Martínez, J. P., Almeida, R., Olmos, S., Rocha, A.P., & Laguna, P. (2004). A wavelet-based ECG delineator evaluation on standard databases. *Institute of Electrical and Electronics Engineers Transactions on Biomedical Engineering*, **51**(4), 570–581.

- Mincholé, A., Zacur, E., Ariga, R., Grau, V., & Rodriguez, B. (2019). MRI-based computational torso/biventricular multiscale models to investigate the impact of anatomical variability on the ECG QRS complex. *Frontiers in Physiology*, **10**, 1103.
- Mountris, K. A., & Pueyo, E. (2021). A dual adaptive explicit time integration algorithm for efficiently solving the cardiac monodomain equation. *International Journal for Numerical Methods in Biomedical Engineering*, **37**(7), e3461.
- Mountris, K. A., Sanchez, C., & Pueyo, E. (2019). A novel paradigm for in silico simulation of cardiac electrophysiology through the mixed collocation meshless Petrov-Galerkin method. In *Computing in cardiology*, IEEE. <https://doi.org/10.22489/CinC.2019.382>.
- Mozos, I., & Serban, C. (2011). The relation between QT interval and T-wave variables in hypertensive patients. *Journal of Pharmacy and Bioallied Sciences*, **3**, 339–344.
- O'Hara, T., Virág, L., Varró, A., & Rudy, Y. (2011). Simulation of the undiseased human cardiac ventricular action potential: Model formulation and experimental validation. *PLoS Computational Biology*, **7**, e1002061.
- Ortigosa, N., Rodriguez-Lopez, M., Bailón, R., Sarvari, S.I., Sitges, M., Gratacós, E., Bijmens, B., Crispi, F., & Laguna, P. (2016). Heart morphology differences induced by intra-uterine growth restriction and preterm birth measured on the ECG at preadolescent age. *Journal of Electrocardiology*, **49**, 401–409.
- Ortigosa, N., Rodriguez-Lopez, M., Bailón, R., Sepulveda-Martinez, A., Gratacós, E., Crispi, F., & Laguna, P. (2018). Intrauterine growth restriction induced ECG morphological differences measured in adulthood. In *Computing in cardiology*. <https://doi.org/10.22489/CinC.2018.302>.
- Pardi, G., & Marconi, A. (1986). The intraventricular conduction time of fetal heart in pregnancies with suspected fetal growth retardation. *British Journal of Obstetrics and Gynaecology*, **93**, 250–254.
- Potse, M., Dubé, B., Richer, J., Vinet, A., & Gulrajani, R. M. (2006). A comparison of monodomain and bidomain reaction-diffusion models for action potential propagation in the human heart. *Institute of Electrical and Electronics Engineers Transactions on Biomedical Engineering*, **53**, 2425–2435.
- Ramírez, J., Orini, M., Tucker, J.D., Pueyo, E., & Laguna, P. (2017). Variability of ventricular repolarization dispersion quantified by time-warping the morphology of the T-waves. *Institute of Electrical and Electronics Engineers Transactions on Biomedical Engineering*, **64**, 1619.
- Ross, M. G., & Beall, M. H. (2008). Adult sequelae of intra-uterine growth restriction. *Seminars in Perinatology*, **32**, 213–218.
- Sarvari, S. I., Rodriguez-Lopez, M., Nuñez-Garcia, M., Sitges, M., Sepulveda-Martinez, A., Camara, O., Butakoff, C., Gratacós, E., Bijmens, B., & Crispi, F. (2017). Persistence of cardiac remodeling in preadolescents with fetal growth restriction. *Circulation: Cardiovascular Imaging*, **10**, e005270.
- Schirone, L., Forte, M., Palmerio, S., Yee, D., Nocella, C., Angelini, F., Pagano, F., Schiavon, S., Bordin, A., Carrizzo, A., Vecchione, C., Valenti, V., Chimenti, I., Falco, E. D., Sciarretta, S., & Frati, G. (2017). A review of the molecular mechanisms underlying the development and progression of cardiac remodeling. *Oxidative Medicine and Cellular Longevity*, **2017**, 3920195.
- Sharma, D., Shastri, S., & Sharma, P. (2016). Intrauterine growth restriction: Antenatal and postnatal aspects. *Clinical Medicine Insights: Pediatrics*, **10**, 67–83.
- Smith, V., Nair, A., Warty, R., Sursas, J. A., da Silva Costa, F., & Wallace, E. M. (2019). A systematic review on the utility of non-invasive electrophysiological assessment in evaluating for intra uterine growth restriction. *BioMed Central Pregnancy and Childbirth*, **19**, 1–14.
- Spach, M. S., Miller 3rd, W., Geselowitz, D. B., Barr, R. C., Kootsey, J. M., & Johnson, E. A. (1981). The discontinuous nature of propagation in normal canine cardiac muscle. Evidence for recurrent discontinuities of intracellular resistance that affect the membrane currents. *Circulation Research*, **48**, 39–54.
- Stewart, P., Aslanidi, O. V., Noble, D., Noble, P. J., Boyett, M. R., & Zhang, H. (2009). Mathematical models of the electrical action potential of purkinje fibre cells. *Philosophical Transactions of the Royal Society A: Mathematical, Physical and Engineering Sciences*, **367**, 2225–2255.
- Szentadrassy, N., Banyasz, T., Biro, T., Szabo, G., Toth, B. I., Magyar, J., Lazar, J., Varro, A., Kovacs, L., & Nanasi, P. P. (2005). Apico-basal inhomogeneity in distribution of ion channels in canine and human ventricular myocardium. *Cardiovascular Research*, **65**, 851–860.
- Van Leeuwen, P., Lange, S., Hackmann, J., Klein, A., Hatzmann, W., & Grönemeyer, D. (2001). Assessment of intra-uterine growth retardation by fetal magnetocardiography. In *Biomag Proceedings of the 12th international conference on biomagnetism, Helsinki, August 13–17, 2000* (pp. 603–606).
- Velayo, C. L., Funamoto, K., Silao, J., Kimura, Y., & Nicolaides, K. (2017). Evaluation of abdominal fetal electrocardiography in early intrauterine growth restriction. *Frontiers in Physiology*, **8**, 437.
- Vijayakumar, M., Fall, C., Osmond, C., & Barker, D. (1995). Birth weight, weight at one year, and left ventricular mass in adult life. *Heart*, **73**, 363–367.
- Visentin, S., Grumolato, F., Nardelli, G. B., Camillo, B. D., Grisan, E., & Cosmi, E. (2014). Early origins of adult disease: Low birth weight and vascular remodeling. *Atherosclerosis*, **237**, 391–399.
- Yamaguchi, M., Shimizu, M., Ino, H., Terai, H., Uchiyama, K., Kotaro, O., Mabuchi, T., Konno, T., Kaneda, T., & Mabuchi, H. (2003). T wave peak-to-end interval and QT dispersion in acquired long QT syndrome: A new index for arrhythmogenicity. *Clinical Science*, **105**, 671–676.

- Zacur, E., Mincholé, A., Villard, B., Carapella, V., Ariga, R., Rodriguez, B., & Grau, V. (2017). MRI-based heart and torso personalization for computer modeling and simulation of cardiac electrophysiology. In *Lecture notes in computer science (including subseries lecture notes in artificial intelligence and lecture notes in bioinformatics)*, LNCS, (Vol. **10549**, pp. 61–70).
- Zaharie, G. C., Hășmășanu, M. G., Blaga, L., Matyas, M., Mureșan, D., Bolboacă, S. D., & Hășmășanu, M. G. (2019). Cardiac left heart morphology and function in newborns with intrauterine growth restriction: Relevance for long-term assessment. *Medical Ultrasonography*, **21**, 62–68.

Additional information

Data availability statement

Clinical data used in this study are available upon reasonable request from the authors of the clinical data acquisition study described in Crispi et al. (2010). The delineation software is publicly available at <https://physionet.org/content/ecgkit/1.0/common/wavedet/>. The models and simulation codes are available at https://github.com/Leo-Bueno/BSICoS-globular_hearts_simulation.

Competing interests

None of the authors has any conflict of interest regarding the submission of this article.

Author contributions

F.L.B.-P. conceptualized and developed the study's methodology, conducted the tests and carried out the formal data analysis. E.Z. contributed to the development of anatomical meshes. E.P.:

analysis of results. F.C.: interpretation of the clinical data. P.L. conceptualized, supervised and planned the methods used in the study. A.M. conceptualized, supervised and planned the methods used in the study. All authors contributed to the writing and editing of the manuscript. All authors have approved the final version of the manuscript and agree to be accountable for all aspects of the work. All persons designated as authors qualify for authorship, and all those who qualify for authorship are listed.

Funding

This work was supported by projects PID2021-128972OA-I00, PID2022-140556OB-I00, CNS2022-135899 and TED2021-130459B-I00 funded by MCIN/AEI, by fellowship RYC2019-027420-I funded by Ramón y Cajal Program, by BSICoS group T39_23R from Aragon government and by PhD scholarship to F.L. Bueno-Palomeque from Fundación Carolina, Universidad de Zaragoza and Universidad Politécnica Salesiana. Computations were performed using ICTS NANBIOSIS (HPC Unit 27).

Keywords

cardiac re-modelling, electrophysiological simulation, IUGR, QRS complex duration, QT interval, sphericity index, T peak-to-end interval, ventricular wall thickness

Supporting information

Additional supporting information can be found online in the Supporting Information section at the end of the HTML view of the article. Supporting information files available:

Peer Review History